Chemical Science

ROYAL SOCIETY OF CHEMISTRY

EDGE ARTICLE

View Article Online
View Journal | View Issue

Cite this: *Chem. Sci.*, 2024, **15**, 10519

All publication charges for this article have been paid for by the Royal Society of Chemistry

Received 31st March 2024
Accepted 28th May 2024

DOI: 10.1039/d4sc02116a

rsc.li/chemical-science

Helical polycyclic hydrocarbons with open-shell singlet ground states and ambipolar redox behaviors†

Qing Jiang, *[a] Hui Tang, [a] Yuchen Peng, [a] Zhenni Hu[a] and Wangdong Zeng*[b]

Organic π-conjugated polycyclic hydrocarbons (PHs) with an open-shell diradical character are attracting increasing interest due to their promising applications in organic electronics and spintronics. However, most of the open-shell PHs synthesized thus far are based on planar π-conjugated molecules. Herein, we report the synthesis and characterization of two new quinodimethane-embedded expanded helicenes **H1** and **H2**. The helical structures of both molecules were revealed using X-ray crystallographic analysis. It was elucidated in detailed experimental and theoretical studies that they possess an open-shell singlet biradical structure in the ground state and show a small energy gap and amphoteric redox behavior. Both compounds can also be easily oxidized or reduced into relatively stable charged species. The dianions of **H1** and **H2** exhibit similar electronic structures to the respective isoelectronic structures of their all-benzenoid helical analogues according to NMR measurements and theoretical calculations. Moreover, the structures of the dication and dianion of **H2** were identified by X-ray crystallographic analysis, revealing the effect of electron transfer on their backbones and aromaticity. This study thus opens up new avenues for both helical polycyclic π-systems and diradicaloids.

Introduction

Organic π-conjugated open-shell polycyclic hydrocarbons (PHs) have attracted a great deal of interest because of their unique optical, electronic, and magnetic properties, which make them promising candidates suitable for functional materials in organic electronic and spintronic devices.[1] According to broken symmetry density functional theory (DFT) calculations, any molecule with a nonzero diradical character in the ground state can be classified as a diradicaloid (diradical-like molecule). It has been demonstrated that the physical properties of open-shell singlet diradicaloids closely correlate with their diradical character.[2] However, PHs with a larger diradical character are expected to show higher reactivity; therefore, instability remains a key obstacle for their practical applications. Over the past few decades, various families of stable diradicaloids based on indenofluorenes,[3] zethrenes,[4] anthenes,[5] bisphenalenyl,[6] and extended quinodimethanes (QDMs)[7] through thermodynamic and kinetic stabilizing strategies have been synthesized to elucidate the interaction of two unpaired electrons and the properties originating from their unique electronic structures. So far, however, most reported open-shell PHs are derived from planar π-conjugated skeletons, and there are only a few examples based on helical systems. For example, cethrene,[8] diindeno-fused bischrysen,[9] 5,14-diaryldiindeno[2,1-*f*:1′,2′-*j*]picene,[10] *para*-QDM embedded double [6]helicene,[11] and dinor [7]helicene[12] were developed by the groups of Juríček, Feng, Wu, Chi, and Stępień, respectively, and these demonstrated an open-shell singlet diradical character and unique electronic properties. Despite these encouraging advances, structural diversity of helical singlet diradicaloids is still limited, which hampers detailed understanding of their electronic structures and properties and the exchange interaction between radicals on the 3D framework. On the other hand, there has been very limited exploration of the effects of electron transfer in these systems, which are of great fundamental importance to understand their electronic and structural responses. In this context, here, we designed and synthesized two novel open-shell helical π-conjugated PHs (**H1** and **H2**) in which one *m*-QDM or π-extended *p*-QDM unit is fused by two phenanthrene rings. We also demonstrated that the recovery of Clar's[13] aromatic sextet rings (the hexagons shaded in blue color in Fig. 1) in the diradical canonical form can serve as a major driving force to form diradicals. For both molecules, two additional aromatic sextet rings can be gained from their closed-shell forms to their diradical forms, and thus, a moderate diradical character can be expected for both molecules. Therefore, they are expected to

[a]*College of Chemistry and Bioengineering, Hunan University of Science and Engineering, Yongzhou 425100, China. E-mail: qjiang198@163.com*

[b]*School of Materials Science and Engineering, Hunan University of Science and Technology, Xiangtan 411201, China. E-mail: wangdong.zeng@hnust.edu.cn*

† Electronic supplementary information (ESI) available: Synthetic procedures, spectroscopic studies, computational analysis and crystal structures. CCDC 2057406, 2057410, 2342019 and 2342022. For ESI and crystallographic data in CIF or other electronic format see DOI: https://doi.org/10.1039/d4sc02116a

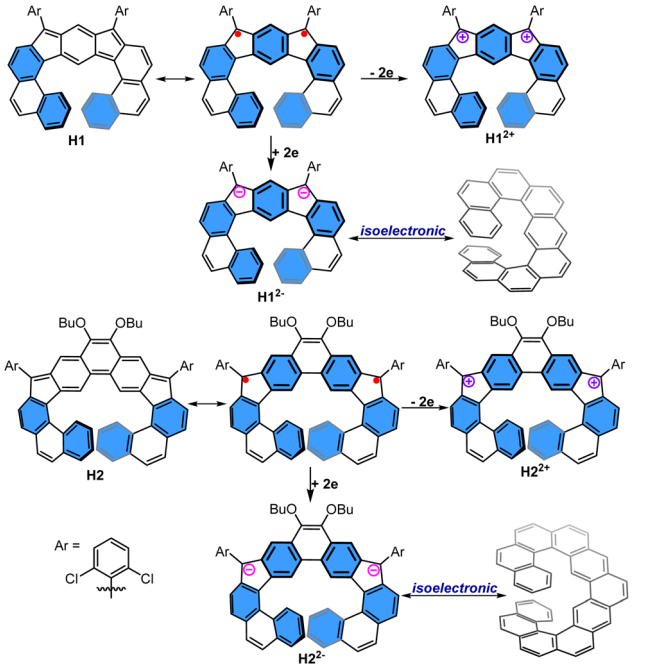

Fig. 1 Representative resonance structures of **H1**/**H2** and their charged species. The structures of all-benzenoid expanded helicenes are also shown.

show significant magnetic characters. Considering their potential open-shell diradical character, bulky and electron deficient 2,6-dichlorophenyl groups are attached onto two cyclopenta (CP) rings to kinetically block the reactive sites. In addition, two-electron oxidation/reduction of the two diradicals may induce aromaticity switching. In particular, their dianions could be regarded as isoelectronic structures of the corresponding all-benzenoid expanded helicenes because of two CP rings in the dianion being aromatic and equal to the benzene ring. Therefore, their aromaticity in neutral and charged forms was discussed, which is also of great interest to understand their unique electronic structures. These characteristics arising from both their helical non-planar structure and aromaticity tunability also make them appealing for photoswitchable applications.[14] In this work, we disclose their synthesis, (anti) aromaticity and magnetic, photophysical and electrochemical properties, together with in-depth elucidation of their redox states.

Results and discussion

Synthesis

The synthesis of **H1** and **H2** was mainly based on a Suzuki coupling and intramolecular Friedel–Crafts alkylation followed by an oxidative dehydrogenation strategy (Scheme 1). First, palladium-catalyzed Suzuki coupling between equimolar amounts of 1-iodo-2-bromobenzene **3** and boronic acid **4** followed by desilylation gave the biphenyl **5** in 86% yield. Subsequent intramolecular cyclization provided the phenanthrene monobromide **6** in 82% yield. Next, palladium-catalyzed Suzuki–Miyaura borylation of **6** gave the key intermediate

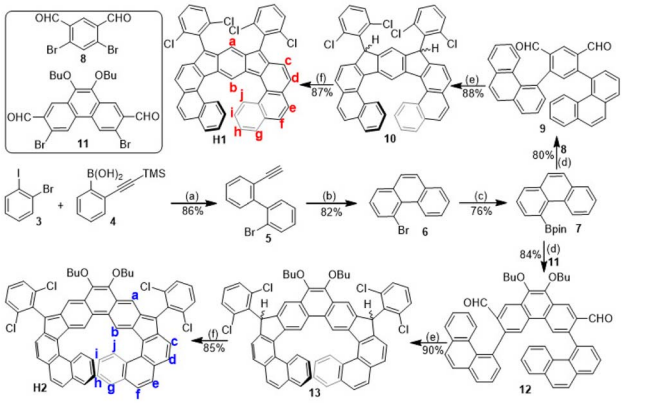

Scheme 1 Synthetic route for **H1** and **H2**: (a) (1) $Pd(PPh_3)_4$, K_2CO_3, THF/H_2O; (2) K_2CO_3, MeOH/DCM; (b) $PtCl_2$, DCE; (c) $B(pin)_2$, Pd(dppf)Cl_2, dioxane; (d) $Pd(PPh_3)_4$, K_2CO_3, THF/H_2O; (e) (1) 2,6-dichloro-1-bromobenzene, isopropylmagnesium chloride, THF; (2) boron trifluoride etherate, DCM; (f) (1) potassium *tert*-butoxide, 18-crown-6, THF; (2) *p*-chloranil.

pinacol borate **7** in 76% yield. Suzuki coupling between **7** and **8** or **11** (ref. [15]) produced the dialdehyde intermediates **9** and **12**, respectively. Treatment of **9**/**12** with 2,6-dichlorophenylmagnesium chloride reagent afforded the corresponding diols, which were subjected to a $BF_3 \cdot OEt_2$-mediated Friedel–Crafts alkylation reaction to generate the dihydro-precursors **10**/**13**. Finally, deprotonation of **10**/**13** by $KOBu^t$ (to generate dianions) followed by oxidization by *p*-chloranil provided the final target compounds **H1** and **H2** in 87% and 85% yield, respectively. The bulky 2,6-dichlorophenyl groups are essential to kinetically block the reactive sites, and also make the final products soluble. Both **H1** and **H2** are stable and can be purified by normal silica gel column chromatography.

X-ray crystallographic analysis

Single crystals suitable for X-ray crystallographic analysis were obtained for **H1** and **H2** by a slow solvent diffusion method.[16] **H1**/**H2** show a helical π-conjugated structure (Fig. 2a and b). The extents of twisting in the helical structures of **H1**/**H2** were obtained by analyzing the corresponding torsion angles, and the geometries of **H1**/**H2** deviate from C_2 symmetry due to the helical twisting, which introduces chirality and asymmetry in the molecule, breaking the C_2 symmetry. As a result, both molecules adopt a C_1 symmetry, which is reflected by the unequal torsion angles of the two cyclopenta-fused [5]helicene substructures. As defined by the selected dihedral angles, the angles of torsion are 21.19° for C1b–C1c–C1d–C1e, 24.08° for C1b′–C1c′–C1d′–C1e′ (Fig. 2a), 21.49° for C2b–C2c–C2d–C2e and 22.17° for C2b′–C2c′–C2d′–C2e′ (Fig. 2b). In **H1**, bonds a (1.430 Å) and d (1.409 Å) are longer than those in typical olefins (1.33–1.34 Å), and there is also large bond length alternation between bonds b (1.449 Å) and c (1.392 Å) in the central benzenoid rings (Fig. 2e), indicating that the molecule still remains a major *s*-indacene sub-structure after annulation with two respective aromatic phenanthrene rings. In **H2**, bonds a (1.407 Å), c (1.398 Å) and d (1.421 Å) are significantly longer

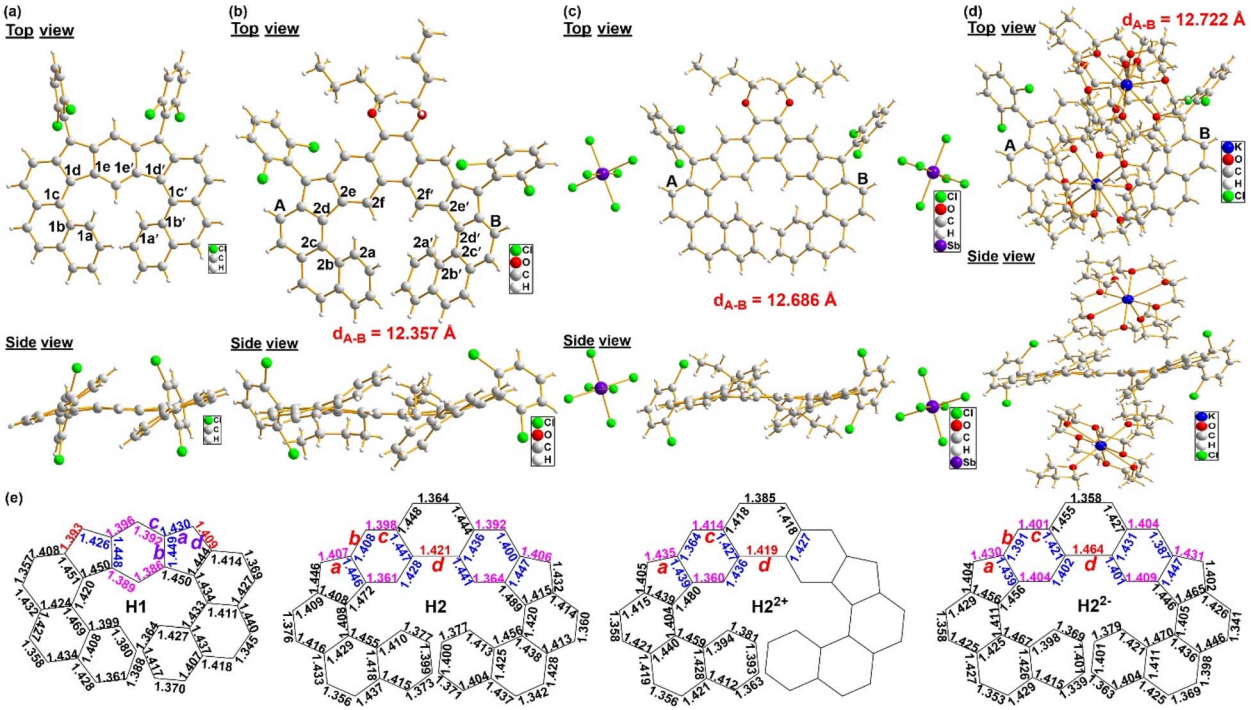

Fig. 2 Top view and side view of the X-ray crystallographic structure of **H1** (a), **H2** (b), [$H2^{2+}\cdot 2SbCl_6^-$] (c) and [$2K^+\cdot H2^{2-}$] (d). (e) Selected bond lengths (in Å) of the backbone of **H**, **H2**, [$H2^{2+}\cdot 2SbCl_6^-$] and [$2K^+\cdot H2^{2-}$].

than those in typical olefins, while bond b (1.408 Å) is much shorter than a typical C(sp^2)–C(sp^2) bond (~1.47 Å) (Fig. 2e), indicating that the quinoidal character of the central extended *para*-quinodimethane unit is diminished by the emergence of the diradical contribution. The above bond length alternation together with the spin populations (Fig. S5†) demonstrates the significant contributions of their diradical resonance structures in the ground state. In the two molecules, the slightly but distinctly different length *exo*-methylene bond a is in accordance with their different singlet diradical character. Indeed, our spin-unrestricted DFT calculations (LC-UBLYP/6-31G(d,p)) predict a diradical character (y_0) of 37.5% and 49.9% for **H1** and **H2**, respectively, in agreement with the bond length analysis.

Interestingly, both **H1** and **H2** contain paired enantiomers (P- and M-type) in the crystals (Fig. S19†), but our attempted resolution using various chiral columns was not successful so far, presumably due to the low racemization energy barrier (Fig. S2†). The racemization processes of **H1** and **H2** were found to proceed through the transition states with face-to-face oriented terminal aromatic rings (Fig. S2†). The transition states adopt a C_s symmetric structure, which is often observed in the transition states of other classical [*n*]helicenes with $n \geq 5$.[17] The calculated racemization barriers from C_2-symmetric P- to M-forms for **H1** and **H2** were 6.1 and 7.4 kcal mol^{-1} at 298 K, respectively, which are much lower than that of classical [*n*] helicene ($n \geq 5$, $\Delta G^{\ddagger} \geq 24.4$ kcal mol^{-1}).[17] On the other hand, there is no π–π interaction between adjacent molecules in the 3D packing structures of **H1**/**H2**, and each molecule is connected to adjacent molecules through intermolecular [C–Cl···π] halogen bonds and [C–H···π] interactions (Fig. S22†).

Magnetic properties

The diradical nature of **H1** and **H2** was explored by variable temperature (VT) proton NMR spectroscopy (Fig. 3). Based on their calculated diradical characters and singlet–triplet gaps, one would expect the need for lower temperatures to observe clear NMR signals. As such, some peaks of **H1** showed broadened ^{1}H NMR signals in THF-d_8 at room temperature, while decreasing the temperature led to sharpened peaks and finally the peaks became clear at 243 K (Fig. 3a). This is strong evidence that the molecule has an open-shell singlet ground state and the NMR broadening is due to the thermal population of triplet species at higher temperatures.[18] For **H2**, its ^{1}H NMR spectra in THF-d_8 at room temperature showed a completely flat baseline for the aromatic region, while the aliphatic region displayed well-resolved butoxyl resonances (Fig. S1†). Upon cooling, some peaks did begin to come up while the aromatic signals still do not gain full resolution even after cooling down to 173 K (Fig. 3b). The aliphatic region in **H2** become broad as the temperature was lowered (Fig. S1†). All of this indicates that the unresolved spectrum of **H2** is a result of two main factors—moderate diradical character and slow configurational flipping at lower temperature (the calculated racemization barrier between the P and M forms of **H2** is 7.4 kcal mol^{-1} at 298 K, Fig. S2†). Similar to the computations, these different results suggest that **H1** and **H2** have very different singlet–triplet energy gaps.

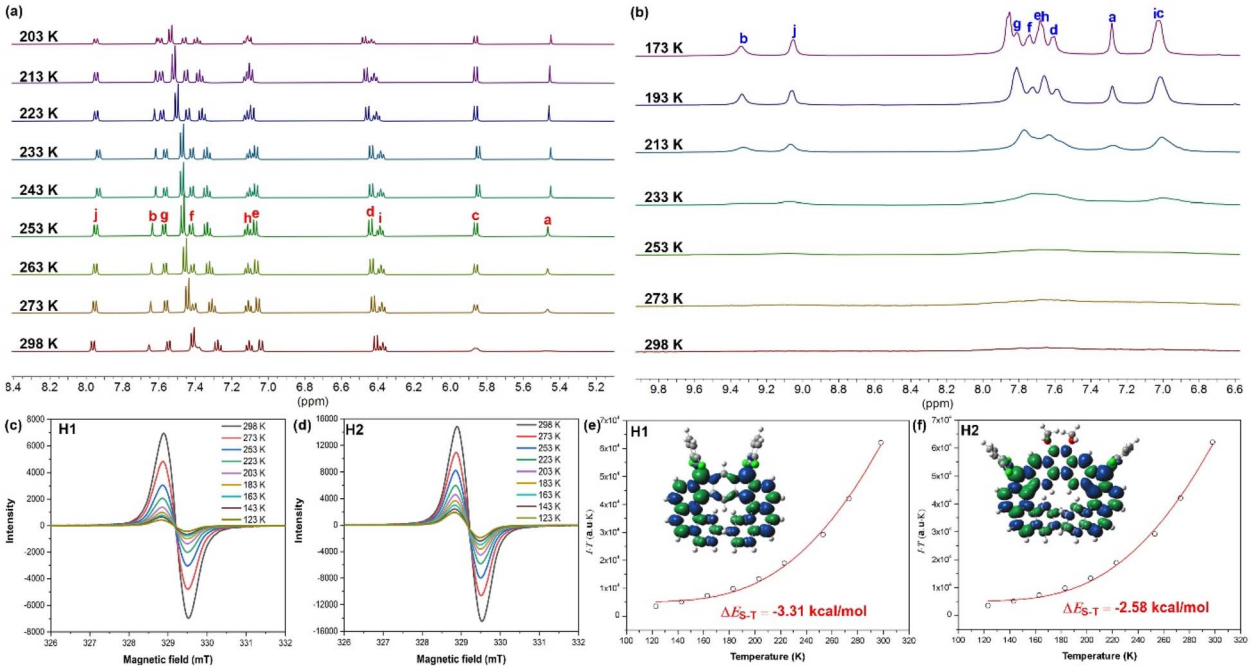

Fig. 3 VT ^{1}H NMR spectra (aromatic region) of **H1** (a) and **H2** (b) in THF-d_8 (refer to Scheme 1 for labelling). VT ESR spectra and fitted $I \times T$–T curves by using the Bleaney–Bowers equation of compounds **H1** (c and e) and **H2** (d and f) in crystalline solid state. Inset is the calculated spin density distribution of the singlet diradical form.

The magnetic properties of both prepared samples were further investigated by variable temperature electron spin resonance (VT ESR) measurements. Strong ESR signals were observed in the crystalline solid at room temperature, and the ESR intensity of **H1** and **H2** decreased with decreasing temperature (Fig. 3c and d), in excellent agreement with their VT NMR data. The ESR signal intensity recorded at different temperatures could be fitted by the Bleaney–Bowers equation[19] to provide a singlet–triplet gap of $\Delta E_{S-T} = -3.31$ and -2.58 kcal mol^{-1} for **H1** and **H2**, respectively (Fig. 3e and f). Furthermore, broken-symmetry DFT calculations (UCAM-B3LYP/6-31(d,p)) also predict that the energies of the open-shell singlet diradical states in **H1**/**H2** are lower than that of the triplet diradical states, with a singlet–triplet energy gap (ΔE_{S-T}) of -1.78 and -1.47 kcal mol^{-1} for **H1** and **H2**, respectively, indicating that they possess an open-shell singlet ground state, which is consistent with the above experimental results.

Optical and electrochemical properties

The optoelectronic properties of **H1** and **H2** were investigated by UV-vis absorption spectroscopy and time-dependent density functional theory (TD DFT) calculations. The new compounds show specific colors in a solution of dichloromethane (see the inset photos in Fig. 4a). These colors originate from intense absorptions in the visible region. The UV-vis absorption spectra of **H1** and **H2** in dichloromethane at room temperature are depicted in Fig. 4a. **H1** shows a well-resolved absorption band with a maximum (λ_{max}) at 750 nm (Fig. 4a), which is significantly redshifted as compared to that of the indeno[2,1-*b*]fluorene derivative (λ_{max} = 638 nm)[3b] due to π-extension. TD DFT

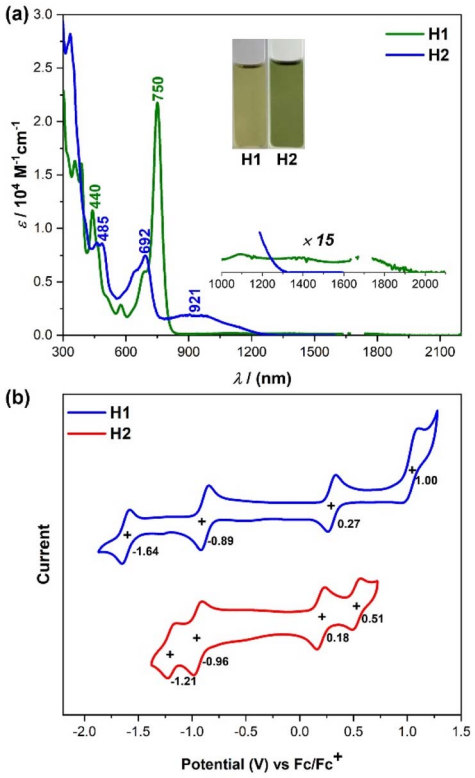

Fig. 4 (a) UV-vis-NIR spectra of **H1** and **H2** in DCM solutions. Inset shows photos of the solutions. (b) Cyclic voltammograms of **H1** and **H2** in DCM solutions.

calculations suggest that this band originates from the HOMO−1 → LUMO electronic transition ($f = 0.4254$) (Fig. S6 and Table S1†). There is another weak broad absorption in the 900–2000 nm region, which mainly originates from the HOMO → LUMO electronic transition ($f = 0.0265$) according to TD DFT calculations (Fig. S6 and Table S1†). The electronic absorption spectrum for **H2** in dichloromethane displays an intense absorption band with λ_{max} at 692 nm and a weak broad absorption in the region of 750–1200 nm (Fig. 4a). Consistent with experimental results, TD DFT calculations predicted a broad absorption at 1362 nm (HOMO → LUMO transition, $f =$ 0.2269) and an intense band at 768 nm (HOMO−1 → LUMO transition, $f = 0.4161$) (Fig. S10 and Table S5†). In addition, the optical energy gaps (E_g^{opt}) of **H1** and **H2** on the basis of the lowest energy absorption onset were roughly estimated to be 0.63 and 0.92 eV, respectively.

To investigate the electrochemical properties of both radicals, cyclic voltammetry and differential pulse voltammetry measurements were carried out in a typical three-electrode electrochemical cell in a solution of tetrabutylammonium hexafluorophosphate (0.1 M) in dry DCM with a scan rate of 100 mV s^{-1} (Fig. 4b). **H1** displayed one reversible oxidation wave and one irreversible oxidation wave with half-wave potential ($E_{1/2}^{ox}$) at 0.26 and 1.00 V, and two reversible reduction waves with half-wave potential ($E_{1/2}^{red}$) at −0.89 and −1.64 V (*vs.* Fc/Fc^+, Fc = ferrocene, Fig. 4b). **H2** exhibited two reversible oxidation waves with $E_{1/2}^{ox} = 0.18$ and 0.51 V and two reversible reduction waves with $E_{1/2}^{red} = -0.96$ and −1.21 V (*vs.* Fc/Fc^+, Fig. 4b). By combining these results with the observed absorption edge, the highest occupied molecular orbital (HOMO) and the lowest unoccupied molecular orbital (LUMO) energy levels of **H1** and **H2** were determined to be −5.00 and −3.99 eV for **H1**, and −4.92 and −3.92 eV for **H2**. Accordingly, the electrochemical energy gaps (E_g^{EC}) are estimated to be 1.01 and 1.00 eV for **H1** and **H2**, respectively, which are consistent with the trend observed in their optical energy band gaps.

Chemical oxidation and reduction

The good redox reversibility from the electrochemical data indicates that both compounds can be easily converted into stable charged species, thus offering the opportunity to investigate optical properties and aromaticity. The first one-electron oxidation of **H1** and **H2** with the oxidant $NO \cdot SbF_6$ gave rise to the corresponding radical cation species. The electronic absorption spectra for $\mathbf{H1}^{\bullet+}$ and $\mathbf{H2}^{\bullet+}$ display a weak broad absorption band in the region of 1500–3000 nm and multiple moderate bands in the visible and near-infrared (NIR) region

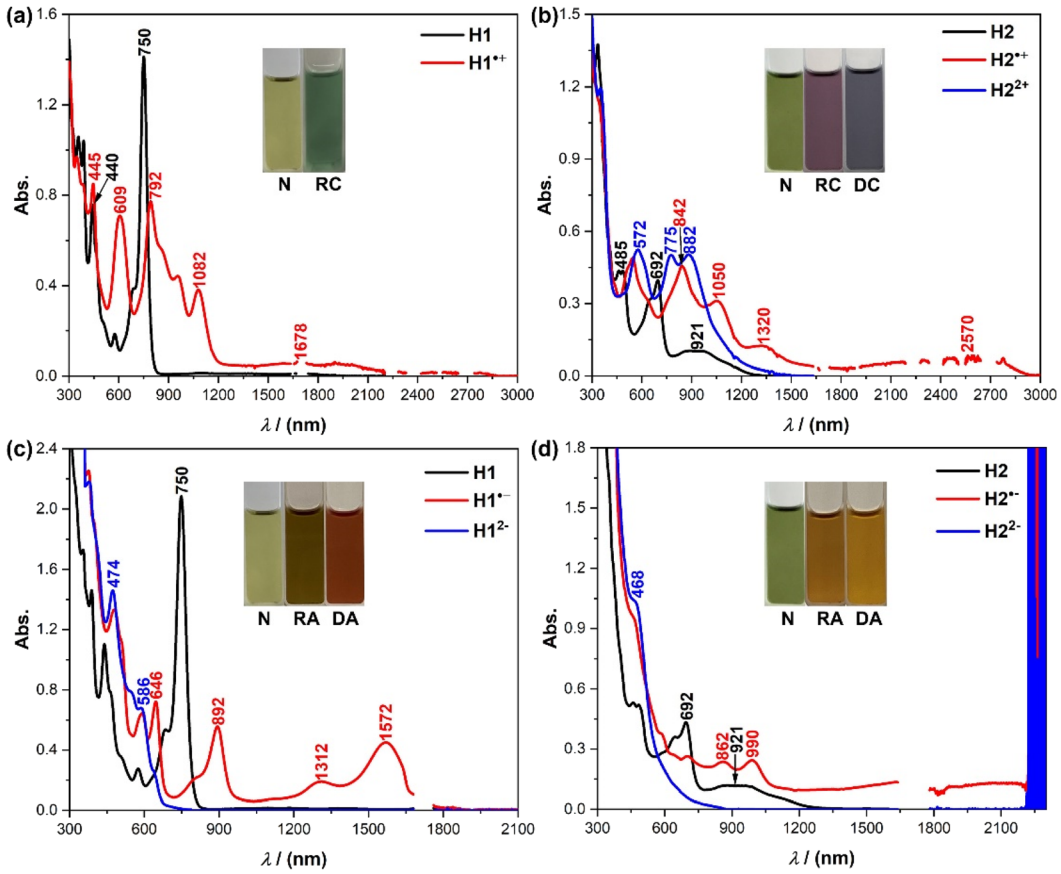

Fig. 5 (a) UV-vis-NIR absorption spectra of **H1** and its radical cation (RC) in DCM. (b) UV-vis-NIR absorption spectra of **H2**, its radical cation (RC) and dication (DC) in DCM. (c) UV-vis-NIR absorption spectra of **H1**, its radical anion (RA) and dianion (DA) in THF. (d) UV-vis-NIR absorption spectra of **H2**, its radical anion (RA) and dianion (DA) in THF; the background absorbance at *ca.* 2250 nm may arise from the overtone of CH vibration of the solvent. Insets show photos of the solutions.

(Fig. 5a and b). Further oxidation of **H1** was not observed even when excess oxidant was added. The second oxidation of **H2** with the oxidant $NO{\cdot}SbF_6$ generated a stable dication species, which exhibits strong shoulder peaks with λ_{max} at 775 and 882 nm (Fig. 5b). The one-electron and two-electron reductions of **H1** and **H2** with freshly prepared sodium anthracenide in dry THF gave their radical anions and dianions, respectively (Fig. 5c and d). The radical anion of **H1** shows an intense absorption band in the NIR region (λ_{max} = 892 and 1572 nm, respectively, Fig. 5c), while the radical anion of **H2** displays long wavelength absorption with a maximum beyond 2200 nm (Fig. 5d). The dianions of **H1** and **H2** exhibit an intense absorption band in the short-wavelength range (λ_{max} = 474 nm for $\mathbf{H1}^{2-}$ and 468 nm for $\mathbf{H2}^{2-}$, Fig. 5c and d). The observed spectra are in agreement with the TD DFT calculations (Fig. S7–S9/S11–S14 and Tables S2–S4/S6–S9†).

The dication of **H2** and the dianions of **H1** and **H2** were *in situ* generated, and all showed sharp ^{1}H NMR spectra at room temperature (Fig. 6 and S3†), thus indicating that all of these charged species possess a closed-shell singlet ground state. The ^{1}H NMR spectra of the dication and dianion of **H2** clearly show that protons b and j are shielded in the dicationic state, whereas protons a, b and j are highly deshielded in the dianionic state (Fig. 6). Similarly, the ^{1}H NMR spectra of the dianion of **H1** clearly show that most of the protons on the backbone appear at low field although the molecule contains two negative charges (Fig. S3†). Single crystals of the dication and dianion of **H2** suitable for X-ray crystallographic analysis were successfully obtained.[16] The X-ray diffraction characterization confirmed the formation of $[\mathbf{H2}^{2+}{\cdot}\mathbf{2SbCl_6}^-]$ (Fig. 2c) and $[\mathbf{2K}^+{\cdot}\mathbf{H2}^{2-}]$ (Fig. 2d), respectively. The dication $[\mathbf{H2}^{2+}{\cdot}\mathbf{2SbCl_6}^-]$ has an axisymmetric structure with two counter cations located at the termini of the conjugated backbone, while the dianion $[\mathbf{2K}^+{\cdot}\mathbf{H2}^{2-}]$ adopts a C_1 symmetry with two counter cations located on the top and bottom of the **H2** molecular plane. In the crystal structure of $[\mathbf{2K}^+{\cdot}\mathbf{H2}^{2-}]$, both K^+ ions are solvent-separated from the $\mathbf{H2}^{2-}$ core, avoiding direct metal ion–π interactions (Fig. 2d). The K^+ ion is axially coordinated to an 18-crown-6 ether molecule ($K{\cdots}O_{crown}$, 2.783–2.832 Å) and capped by two THF molecules ($K{\cdots}O_{THF}$, 2.670–2.693 Å), with all $K{\cdots}O$ distances being close to those previously reported.[20] The lengths of bond a in the dication and dianion of **H2** are 1.435 and 1.430 Å (Fig. 2e), respectively, which are much larger than that of a neutral molecule. A comparison of selected angles (Fig. 2) reveals that **H2** exhibits structural deformation upon the addition or loss of two electrons. The torsion angle for C2b–C2c–C2d–C2e decreases from 21.49° in **H2** to 12.90° in $\mathbf{H2}^{2+}$ and 18.01° in $\mathbf{H2}^{2-}$, respectively. Thus, the central helicene axis is compressed upon two-electron oxidation or reduction. In order to balance the resulting intramolecular steric hindrance, the helicene core (d_{A-B}, Fig. 2) is lengthened from 12.357 Å in **H2** to 12.686 Å in $\mathbf{H2}^{2+}$ and 12.722 Å in $\mathbf{H2}^{2-}$, respectively.

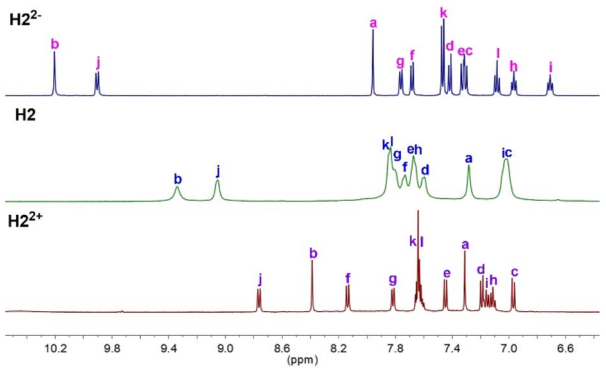

Fig. 6 ^{1}H NMR spectra (aromatic region) of **H2** (in CD_2Cl_2), $\mathbf{H2}^{2+}$ (in CD_2Cl_2), and $\mathbf{H2}^{2-}$ (in [D_8]THF) (refer to Scheme 1 for labelling).

DFT calculations

To deeply understand the NMR spectra and the difference of the (anti)aromaticity of individual rings at different redox states, nucleus independent chemical shift (NICS)[21] and anisotropy of the induced current density (ACID)[22] calculations were conducted at the CAM-B3LYP/6-31G(d,p) level of theory based on similar previous computational studies on large polycyclic systems.[23] For the neutral compound **H1**, the three rings in the *s*-indacene unit have positive NICS(1)$_{zz}$ values (57.81–70.93, *i.e.*, antiaromatic), the neighbouring benzenoid rings have also positive NICS(1)$_{zz}$ values (8.58), while the terminal naphthalene rings have negative NICS(1)$_{zz}$ values (−10.86 to −27.22, *i.e.*, aromatic) (Fig. 7a). The ACID plot shows clockwise diatropic ring current flow along the terminal naphthalene units (aromatic), counter-clockwise paratropic ring current for the three rings in the *s*-indacene unit (antiaromatic), and there is counter-clockwise paratropic ring current for the benzenoid rings near the *s*-indacene unit (antiaromatic) (Fig. 7b), in accordance with the NICS(1)$_{zz}$ results. Accordingly, proton a in **H1** appears at high field due to the shielding effect from the anti-aromatic *s*-indacene unit, while proton b in **H1** appears at low field due to the deshielding effect from the aromatic naphthalene ring (Fig. 3a). For **H2**, the terminal phenanthrene rings have negative NICS(1)$_{zz}$ values (−12.75 to −29.14) and the CP rings have positive NICS(1)$_{zz}$ values (21.75), while the central benzenoid ring has a NICS(1)$_{zz}$ value of 0.87 (nearly non-aromatic) (Fig. 7a). The ACID plot displays clockwise diatropic ring current flow along the terminal phenanthrene units and counter-clockwise paratropic ring current at the CP rings, while there is almost no clear ring current for the central benzenoid ring (Fig. 7d). Accordingly, proton a in **H2** appears at high field due to the shielding effect from the anti-aromatic CP ring, while proton b in **H2** appears at low field due to the deshielding effect from the aromatic phenanthrene ring (Fig. 3b). NICS and ACID calculations of the dication $\mathbf{H2}^{2+}$ reveal the aromatic character of the terminal benzene rings, while the nearby benzene rings are nearly non-aromatic (Fig. 7a and e). The two CP rings are anti-aromatic with counter-clockwise paratropic ring current and positive NICS(1)$_{zz}$ values (44.64), while the central benzenoid ring is nearly non-aromatic. Accordingly, proton b in $\mathbf{H2}^{2+}$ is shielded by the antiaromatic CP rings (Fig. 6). The ACID plot and NICS values of the dianion $\mathbf{H2}^{2-}$ (Fig. 7a and f) disclose that all rings are aromatic with negative NICS(1)$_{zz}$ values (−9.83 to −28.72), and π electrons are mainly delocalized along the

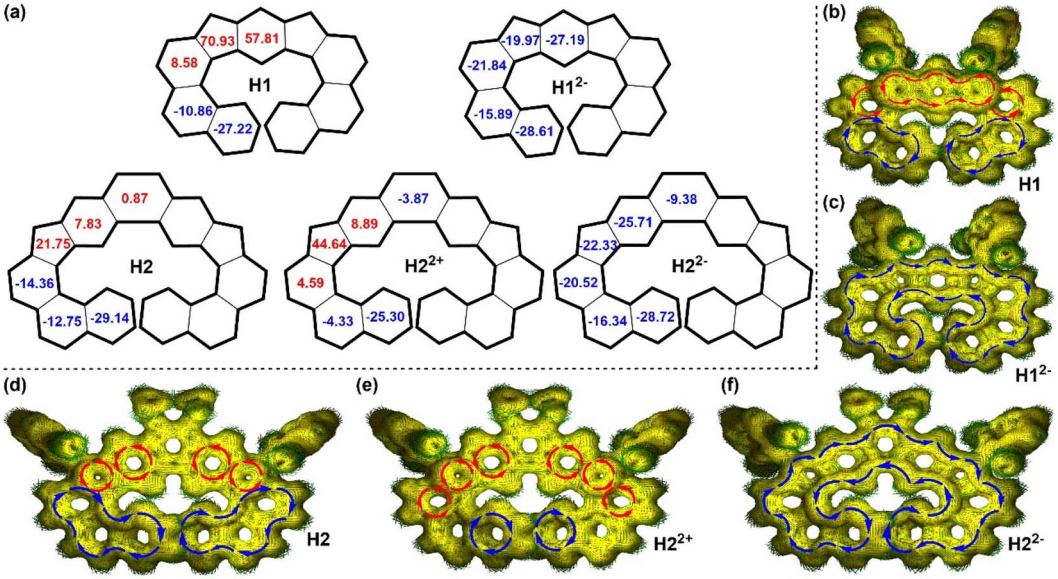

Fig. 7 (a) NICS(1)$_{zz}$ values (the numbers in the rings) of **H1**, **H1**$^{2-}$, **H2**, **H2**$^{2+}$ and **H2**$^{2-}$ calculated at the CAM-B3LYP/6-31G(d,p) level. ACID plots of **H1** (b), **H1**$^{2-}$ (c), **H2** (d), **H2**$^{2+}$ (e), and **H2**$^{2-}$ (f) calculated at the CAM-B3LYP/6-31G(d,p) level. The red and blue arrows indicate the counter-clockwise (paratropic) and clockwise (diatropic) current flow, respectively.

periphery with a clockwise current flow. Accordingly, protons a, b and j in **H2**$^{2-}$ are deshielded by the whole aromatic backbone (Fig. 6). For **H1**$^{2-}$, each individual ring has negative NICS(1)$_{zz}$ values (−15.89 to −28.61, Fig. 7a), and a diatropic ring current circuit along the periphery is formed in the calculated ACID plot (Fig. 7c). In addition, NICS and ACID calculations of the corresponding all-benzenoid analogues show that the π-electrons can also form clockwise diatropic ring currents along the periphery of the backbone (Fig. S15†). Thus, the dianions of **H1** and **H2** can be regarded as the isoelectronic structures of the corresponding all-benzenoid expanded helicenes. All of this suggests that in dianions a global electron delocalization is obtained, leading to global aromaticity in the whole structure, while in the case of the neutral structures and dication the current-density pathways are composed of local aromatic and antiaromatic units. On the other hand, the calculated electrostatic potential maps (Fig. S16 and S17†) suggest that the charges are well delocalized along the entire backbone to minimize Coulomb repulsion. Hirshfeld charge distribution (Fig. S18 and S19†) shows that the head carbons of CP rings in **H2**$^{2+}$ and **H2**$^{2-}$ have the highest charge densities, while the negative charges of **H1**$^{2-}$ are primarily distributed along the periphery with C18 and C31 atoms having the largest negative charge densities.

Conclusions

In summary, we have synthesized two helical π-conjugated diradicaloids **H1** and **H2** by fusion of a QDM unit with two phenanthrene rings at the termini, and their electronic structure and geometry in the ground state were investigated by various experiments assisted by DFT calculations. Single crystal X-ray analysis discloses that **H1** and **H2** have a helical molecular configuration. Due to the anti-aromatic character and quinoidal character of the central units, they exhibit open-shell diradical character and magnetic activity. Moreover, the dication of **H2** is experimentally accessible by chemical oxidation with NO·SbF$_6$, thus displaying a closed-shell ground electron state and a local aromatic character. The dianions of **H1** and **H2** were also obtained, showing similar electronic structures to their respective isoelectronic structures, the all-benzenoid expanded [9]helicene and [11]helicene. The successful X-ray structural characterization of the charged products reaffirms the structural flexibility of **H2** driven by electron transfer processes and reveals a notable helical core compression upon two-electron oxidation or reduction. As a result of their intrinsic chirality, electronic and magnetic properties, as well as redox activities, these molecules could hold promise for chirality-induced spin selectivity, field-effect transistors, energy storage, and spintronics. This study not only opens up a new avenue for helical polycyclic π-systems, but also provides important insights into the construction of stable chiral diradicaloids for organic-based magneto-optical devices and magnetic chiral dichroism.

Computational details

All geometries were fully optimized using the B3LYP or CAM-B3LYP functionals, in combination with the 6-31G(d,p) basis set.[24,25] Natural orbital occupation number (NOON) calculations were done by a spin unrestricted LC-BLYP/6-31G(d) method and the diradical character (y_0) was calculated according to Yamaguchi's scheme: $y_0 = 1 - (2T/(1 + T^2))$, and $T = (n_{HONO} - n_{LUNO})/2$ (where n_{HONO} is the occupation number of the HONO, and n_{LUNO} is the occupation number of the LUNO).[26] Calculations of single point energies, molecular orbitals and time-dependent DFT (TD-DFT) for all DFT-optimized structures were obtained

by using the B3LYP/6-31G(d,p). Given that hybrid long-range corrected functionals like CAM-B3LYP are well suited for describing electron delocalization in large polycyclic systems[23] and provide magnetic properties consistent with those obtained at the CCSD(T) level,[27] we chose the CAM-B3LYP/6-31G(d,p) level of theory for NICS and ACID calculations. NICS values were calculated using the standard GIAO procedure.[21,28] An ACID plot was calculated by using the method developed by Herges.[22,29] Electrostatic potential maps and Hirshfeld charges were calculated at the B3LYP/6-31G(d,p). In the study of racemization processes, the molecular geometries of all stationary points were optimized at the B3LYP level of DFT with the 6-31G(d) basis set with the IEPCM model for solvation of THF at 298 K. Harmonic vibration frequency calculations at the same level were performed to verify all stationary points as local minima (with no imaginary frequency) and transition states (with one imaginary frequency). IRC calculations[30] were also performed to check transition states.

Data availability

The experimental procedures, characterizations, spectral analysis and DFT computational details are available in the ESI.†

Author contributions

Q. Jiang and W. Zeng supervised and designed the project. Q. Jiang, H. Tang, Y. Peng and Z. Hu synthesized and characterized the compounds. All authors discussed the results and contributed to the manuscript writing.

Conflicts of interest

There are no conflicts to declare.

Acknowledgements

Q. Jiang acknowledges the construct program of applied characteristic discipline in Hunan Province and the High-level Talent Program from Hunan University of Science and Engineering for financial support. W. Zeng is thankful for the financial support from the National Natural Science Foundation of China (Grant No. 22175061), Excellent Youth Foundation of Hunan Scientific Committee (Grant No. 2022JJ10025), Key research and development projects of Hunan Province (Grant No. 2022GK2035) and Key research and development projects of Xiangtan City (Grant No. ZX-ZD20221006).

Notes and references

1 (*a*) X. Hu, W. Wang, D. Wang and Y. Zheng, *J. Mater. Chem. C*, 2018, **6**, 11232; (*b*) Y. Tobe, *Top. Curr. Chem.*, 2018, **376**, 1; (*c*) T. Kubo, *Chem. Lett.*, 2015, **44**, 111; (*d*) Z. Zeng, X. Shi, C. Chi, J. T. López Navarrete, J. Casado and J. Wu, *Chem. Soc. Rev.*, 2015, **44**, 6578; (*e*) M. Abe, Diradicals, *Chem. Rev.*, 2013, **113**, 7011; (*f*) Z. Sun, Q. Ye, C. Chi and J. Wu, *Chem. Soc. Rev.*, 2012, **41**, 7857; (*g*) A. Rajca, *Chem. Rev.*, 1994, **94**, 871; (*h*) T. Y. Gopalakrishna, W. Zeng, X. Lu and J. Wu, *Chem. Commun.*, 2018, **54**, 2186; (*i*) Z. Sun, Z. Zeng and J. Wu, *Acc. Chem. Res.*, 2014, **47**, 2582.

2 K. Yamaguchi, *Chem. Phys. Lett.*, 1975, **33**, 330.

3 (*a*) C. K. Frederickson, B. D. Rose and M. M. Haley, *Acc. Chem. Res.*, 2017, **50**, 977; (*b*) A. Shimizu, R. Kishi, M. Nakano, D. Shiomi, K. Sato, T. Takui, I. Hisaki, M. Miyata and Y. Tobe, *Angew. Chem., Int. Ed.*, 2013, **52**, 6076; (*c*) J. Dressler, Z. Zhou, J. Marshall, R. Kishi, S. Takamuku, Z. Wei, S. Spisak, M. Nakano, M. Petrukhina and M. M. Haley, *Angew. Chem., Int. Ed.*, 2017, **48**, 15363; (*d*) S. Qiu, C. Wang, S. Xie, X. Huang, L. Chen, Y. Zhao and Z. Zeng, *Chem. Commun.*, 2018, **54**, 11383; (*e*) D. T. Chase, A. G. Fix, S. J. Kang, B. D. Rose, C. D. Weber, Y. Zhong, L. N. Zakharov, M. C. Lonergan, C. Nuckolls and M. M. Haley, *J. Am. Chem. Soc.*, 2012, **134**, 10349.

4 (*a*) P. Hu and J. Wu, *Can. J. Chem.*, 2017, **95**, 223; (*b*) W. Zeng, T. Y. Gopalakrishna, H. Phan, T. Tanaka, T. S. Herng, J. Ding, A. Osuka and J. Wu, *J. Am. Chem. Soc.*, 2018, **140**, 14054; (*c*) Z. Sun, S. Lee, K. H. Park, X. Zhu, W. Zhang, B. Zheng, P. Hu, Z. Zeng, S. Das, Y. Li, C. Chi, R.-W. Li, K.-W. Huang, J. Ding, D. Kim and J. Wu, *J. Am. Chem. Soc.*, 2013, **135**, 18229; (*d*) W. Zeng, Z. Sun, T. S. Herng, T. P. Goncalves, T. Y. Gopalakrishna, K.-W. Huang, J. Ding and J. Wu, *Angew. Chem., Int. Ed.*, 2016, **55**, 8615; (*e*) Y. Li, W. K. Heng, B. S. Lee, N. Aratani, J. L. Zafra, N. Bao, R. Lee, Y. M. Sung, Z. Sun, K. W. Huang, R. D. Webster, J. T. L. Navarrete, D. Kim, A. Osuka, J. Casado, J. Ding and J. Wu, *J. Am. Chem. Soc.*, 2012, **134**, 14913; (*f*) Z. Sun, W. Fan, Y. Han, W. Yuan, Y. Ni, J. Wang, H. Wei, Y. Zhao, Z. Sun and J. Wu, *Chem. Sci.*, 2023, **14**, 7922; (*g*) C. Zong, S. Yang, Y. Sun, L. Zhang, J. Hu, W. Hu, R. Li and Z. Sun, *Chem. Sci.*, 2022, **13**, 11442; (*h*) C. Zong, X. Zhu, Z. Xu, L. Zhang, J. Xu, J. Guo, Q. Xiang, Z. Zeng, W. Hu, J. Wu, R. Li and Z. Sun, *Angew. Chem., Int. Ed.*, 2021, **60**, 16230.

5 (*a*) A. Konishi, Y. Hirao, H. Kurata, T. Kubo, M. Nakano and K. Kamada, *Pure Appl. Chem.*, 2014, **86**, 497; (*b*) A. Konishi, Y. Hirao, K. Matsumoto, H. Kurata, R. Kishi, Y. Shigeta, M. Nakano, K. Tokunaga, K. Kamada and T. Kubo, *J. Am. Chem. Soc.*, 2013, **135**, 1430; (*c*) A. Konishi, Y. Hirao, M. Nakano, A. Shimizu, E. Botek, B. Champagne, D. Shiomi, K. Sato, T. Takui, K. Matsumoto, H. Kurata and T. Kubo, *J. Am. Chem. Soc.*, 2010, **132**, 11021.

6 (*a*) A. Shimizu, T. Kubo, M. Uruichi, K. Yakushi, M. Nakano, D. Shiomi, K. Sato, T. Takui, Y. Hirao, K. Matsumoto, H. Kurata, Y. Morita and K. Nakasuji, *J. Am. Chem. Soc.*, 2010, **132**, 14421; (*b*) T. Kubo, M. Sakamoto, M. Akabane, Y. Fujiwara, K. Yamamoto, M. Akita, K. Inoue, T. Takui and K. Nakasuji, *Angew. Chem., Int. Ed.*, 2004, **43**, 6474; (*c*) A. Shimizu, M. Uruichi, K. Yakushi, H. Matsuzaki, H. Okamoto, M. Nakano, Y. Hirao, K. Matsumoto, H. Kurata and T. Kubo, *Angew. Chem., Int. Ed.*, 2009, **48**, 5482; (*d*) T. Kubo, A. Shimizu, M. Sakamoto, M. Uruichi, K. Yakushi, M. Nakano, D. Shiomi, K. Sato, T. Takui, Y. Morita and K. Nakasuji, *Angew. Chem., Int. Ed.*, 2005, **44**, 6564; (*e*) A. Shimizu, Y. Hirao, K. Matsumoto, H. Kurata,

T. Kubo, M. Uruichi and K. Yakushi, *Chem. Commun.*, 2012, **48**, 5629.

7 (*a*) Q. Jiang, T. Tao, H. Phan, Y. Han, T. Y. Gopalakrishna, T. S. Herng, G. Li, L. Yuan, J. Ding and C. Chi, *Angew. Chem., Int. Ed.*, 2018, **57**, 16737; (*b*) J. Casado, *Top. Curr. Chem.*, 2017, **375**, 73; (*c*) C. KFrederickson, B. D. Rose and M. M. Haley, *Acc. Chem. Res.*, 2017, **50**, 977; (*d*) X. Shi, P. M. Burrezo, S. Lee, W. Zhang, B. Zheng, G. Dai, J. J. Chang, T. López Navarrete, K.-W. Huang, D. Kim, J. Casado and C. Chi, *Chem. Sci.*, 2014, **5**, 4490; (*e*) J. E. Barker, J. J. Dressler, A. Cárdenas Valdivia, R. Kishi, E. T. Strand, L. N. Zakharov, S. N. MacMillan, C. J. Gómez-García, M. Nakano, J. Casado and M. M. Haley, *J. Am. Chem. Soc.*, 2020, **142**, 1548; (*f*) S. Dong, T. S. Herng, T. Y. Gopalakrishna, H. Phan, Z. L. Lim, P. Hu, R. D. Webster, J. Ding and C. Chi, *Angew. Chem., Int. Ed.*, 2016, **55**, 9316; (*g*) Z. Zeng and J. Wu, *Chem. Rec.*, 2015, **15**, 322; (*h*) M. A. Majewski, P. J. Chmielewski, A. Chien, Y. H. Tadeusz Lis, M. Witwicki, D. Kim, P. M. Zimmerman and M. Stepien, *Chem. Sci.*, 2019, **10**, 3413; (*i*) H. Hayashi, J. E. Barker, A. C. Valdivia, R. Kishi, S. N. MacMillan, C. J. Gómez-García, H. Miyauchi, Y. Nakamura, M. Nakano, S.-I. Kato, M. M. Haley and J. Casado, *J. Am. Chem. Soc.*, 2020, **142**(48), 20444; (*j*) J. Guo, Z. Li, X. Tian, T. Zhang, Y. Wang and C. Dou, *Angew. Chem., Int. Ed.*, 2023, **62**, e202217470; (*k*) J. Guo, Y. Yang, C. Dou and Y. Wang, *J. Am. Chem. Soc.*, 2021, **143**(43), 18272.

8 (*a*) P. Ravat, T. Šolomek, D. Haussinger, O. Blacque and M. Juríček, *J. Am. Chem. Soc.*, 2018, **140**, 10839; (*b*) T. Šolomek, P. Ravat, Z. Mou, M. Kertesz and M. Juríček, *J. Org. Chem.*, 2018, **83**, 4769; (*c*) P. Ravat, T. Šolomek, M. Rickhaus, D. Haussinger, M. Neuburger, M. Baumgarten and M. Juríček, *Angew. Chem., Int. Ed.*, 2016, **55**, 1183.

9 (*a*) J. Ma, J. Liu, M. Baumgarten, Y. Fu, Y.-Z. Tan, K. S. Schellhammer, F. Ortmann, G. Cuniberti, H. Komber, R. Berger, K. Müllen and X. Feng, *Angew. Chem., Int. Ed.*, 2017, **56**, 3280; (*b*) J. Ma, K. Zhang, K. S. Schellhammer, Y. Fu, H. Komber, C. Xu, A. A. Popov, F. Hennersdorf, J. J. Weigand, S. Zhou, W. Pisula, F. Ortmann, R. Berger, J. Liu and X. Feng, *Chem. Sci.*, 2019, **10**, 4025.

10 Y.-C. Hsieh, C.-F. Wu, Y.-T. Chen, C.-T. Fang, C.-S. Wang, C.-H. Li, L.-Y. Chen, M.-J. Cheng, C.-C. Chueh, P.-T. Chueh and Y.-T. Wu, *J. Am. Chem. Soc.*, 2018, **140**, 14357.

11 Q. Jiang, Y. Han, Y. Zou, H. Phan, L. Yuan, T. S. Herng, J. Ding and C. Chi, *Chem.–Eur. J.*, 2020, **26**, 15613.

12 A. Borissov, P. J. Chmielewski, C. J. Gómez García, T. Lis and M. Stępień, *Angew. Chem., Int. Ed.*, 2023, **62**, e202309238.

13 E. Clar, *The Aromatic Sextet*, Wiley, New York, 1972.

14 (*a*) M. Mauksch and S. Tsogoeva, *Chem.–Eur. J.*, 2021, **27**, 14660; (*b*) M. Orozco-Ic, R. R. Valiev and D. Sundholm, *Phys. Chem. Chem. Phys.*, 2022, **24**, 6404; (*c*) M. Orozco-Ic, L. Soriano-Agueda, S. Escayola, D. Sundholm, G. Merino and E. Matito, *J. Org. Chem.*, 2024, **89**, 2459; (*d*) H. Kubo, D. Shimizu, T. Hirose and K. Matsuda, *Org. Lett.*, 2020, **22**, 9276; (*e*) E. Cherni, B. Champagne, S. Ayadi and V. Liégeois, *Phys. Chem. Chem. Phys.*, 2019, **21**, 14678; (*f*) M. Orozco-Ic, J. Barroso, N. D. Charistos, A. Muñoz-Castro and G. Merino, *Chem.–Eur. J.*, 2020, **26**, 326; (*g*) C. K. Frederickson, L. N. Zakharov and M. M. Haley, *J. Am. Chem. Soc.*, 2016, **138**, 16827; (*h*) G. I. Warren, J. E. Barker, L. N. Zakharov and M. M. Haley, *Org. Lett.*, 2021, **23**, 5012.

15 X. Lu, T. Y. Gopalakrishna, H. Phan, T. S. Herng, Q. Jiang, C. Liu, G. Li, J. Ding and J. Wu, *Angew. Chem., Int. Ed.*, 2018, **57**, 13052.

16 Deposition numbers 2057406 (**H1**), 2057410 (**H2**), 2342019 ($\mathbf{H2}^{2+}$) and 2342022 ($\mathbf{H2}^{2-}$) contain the supplementary crystallographic data for this paper. These data are provided free of charge by The Cambridge Crystallographic Data Centre.†

17 J. Barroso, J. L. Cabellos, S. Pan, F. Murillo, X. Zarate, M. A. Fernandez-Herrera and G. Merino, *Chem. Commun.*, 2018, **54**, 188.

18 (*a*) S. Dong, T. S. Herng, T. Y. Gopalakrishna, H. Phan, Z. L. Lim, P. Hu, R. D. Webster, J. Ding and C. Chi, *Angew. Chem., Int. Ed.*, 2016, **55**, 9316; (*b*) S. Dong, T. Y. Gopalakrishna, Y. Han, H. Phan, T. Tao, Y. Ni, G. Liu and C. Chi, *J. Am. Chem. Soc.*, 2019, **141**, 62; (*c*) T. Xu, Y. Han, Z. Shen, X. Hou, Q. Jiang, W. Zeng, P. W. Ng and C. Chi, *J. Am. Chem. Soc.*, 2021, **143**, 20562; (*d*) A. Ong, T. Tao, Q. Jiang, Y. Han, Y. Ou, K.-W. Huang and C. Chi, *Angew. Chem., Int. Ed.*, 2022, **61**, e202209286; (*e*) Z. Li, X. Hou, Y. Han, W. Fan, Y. Ni, Q. Zhou, J. Zhu, S. Wu, K.-W. Huang and J. Wu, *Angew. Chem., Int. Ed.*, 2022, **61**, e202210697; (*f*) T. Xu, X. Hou, Y. Han, H. Wei, Z. Li and C. Chi, *Angew. Chem., Int. Ed.*, 2023, **62**, e202304937; (*g*) W. Kueh, X. Shi, T. W. Phua, H. Kueh, Y. C. Liau and C. Chi, *Org. Lett.*, 2022, **24**, 5935; (*h*) J.-J. Shen, Y. Han, S. Dong, H. Phan, T. S. Herng, T. Xu, J. Ding and C. Chi, *Angew. Chem., Int. Ed.*, 2021, **60**, 4464; (*i*) Q. Jiang, H. Wei, X. Hou and C. Chi, *Angew. Chem., Int. Ed.*, 2023, **62**, e202306938; (*j*) Q. Jiang, Y. Han, Y. Zou and C. Chi, *J. Mater. Chem. C*, 2023, **11**, 15160.

19 B. Bleaney and K. D. Bowers, *Proc. R. Soc. London, Ser. A*, 1952, **214**, 451.

20 (*a*) Z. Zhou, X.-Y. Wang, Z. Wei, K. Müllen and M. A. Petrukhina, *Angew. Chem., Int. Ed.*, 2019, **58**, 14969; (*b*) Z. Zhou, R. K. Kawade, Z. Wei, F. Kuriakose, O. Ungor, M. Jo, M. Shatruk, R. Gershoni-Poranne, M. A. Petrukhina and I. V. Alabugin, *Angew. Chem., Int. Ed.*, 2020, **59**, 1256; (*c*) S. N. Spisak, A. Yu. Rogachev, A. V. Zabula, A. S. Filatov, R. Clérac and M. A. Petrukhina, *Chem. Sci.*, 2017, **8**, 3137; (*d*) Z. Zhou, L. Fu, Y. Hu, X.-Y. Wang, Z. Wei, A. Narita, K. Müllen and M. A. Petrukhina, *Angew. Chem., Int. Ed.*, 2020, **59**, 15923.

21 Z. Chen, C. S. Wannere, C. Corminboeuf, R. Puchta and P. V. R. Schleyer, *Chem. Rev.*, 2005, **105**, 3842.

22 D. Geuenich, K. Hess, F. Köhler and R. Herges, *Chem. Rev.*, 2005, **105**, 3758.

23 (*a*) L. J. Karas, S. Jalife, R. V. Viesser, J. V. Soares, M. M. Haley and J. I. Wu, *Angew. Chem., Int. Ed.*, 2023, **62**, e202307379; (*b*) I. Casademont-Reig, R. Guerrero-Avilés, E. Ramos-Cordoba, M. Torrent-Sucarrat and E. Matito, *Angew. Chem., Int. Ed.*, 2021, **60**, 24080; (*c*) D. W. Szczepanik, M. Solà,

M. Andrzejak, B. Pawełek, K. Dyduch, M. Kukułka, T. M. Krygowski and H. Szatylowicz, *J. Comput. Chem.*, 2017, **38**, 1640; (*d*) D. Inostroza, V. García, O. Yañez, J. J. Torres-Vega, A. Vásquez-Espinal, R. Pino-Rios, R. Báez-Grez and W. Tiznado, *New J. Chem.*, 2021, **45**, 8345; (*e*) M. Orozco-Ic and G. Merino, *Chemistry*, 2021, **3**, 1381; (*f*) M. Orozco-Ic, M. Dimitrova, J. Barroso, D. Sundholm and G. Merino, *J. Phys. Chem. A*, 2021, **125**, 5753; (*g*) I. Casademont-Reig, E. Ramos-Cordoba, M. Torrent-Sucarrat and E. Matito, *Molecules*, 2020, **25**, 711; (*h*) M. Orozco-Ic and D. Sundholm, *Phys. Chem. Chem. Phys.*, 2022, **24**, 22487.

24 F. P. Gasparro and N. H. Kolodny, *J. Chem. Educ.*, 1977, **54**, 258.

25 T. Yanai, D. P. Tew and N. C. Handy, *Chem. Phys. Lett.*, 2004, **393**, 51.

26 (*a*) A. D. Becke, *J. Chem. Phys.*, 1993, **98**, 5648; (*b*) C. Lee, W. Yang and R. G. Parr, *Phys. Rev. B: Condens. Matter*, 1988, **37**, 785; (*c*) R. Ditchfield, W. J. Hehre and J. A. Pople, *J. Chem. Phys.*, 1971, **54**, 724; (*d*) W. J. Hehre, R. Ditchfield and J. A. Pople, *J. Chem. Phys.*, 1972, **56**, 2257; (*e*) P. C. Hariharan and J. A. Pople, *Theor. Chim. Acta*, 1973, **28**, 213.

27 S. Lehtola, M. Dimitrova, H. Fliegl and D. Sundholm, *J. Chem. Theory Comput.*, 2021, **17**, 1457.

28 (*a*) S. Yamanaka, M. Okumura, M. Nakano and K. Yamaguchi, *J. Mol. Struct.*, 1994, **310**, 205; (*b*) K. Kamada, K. Ohta, A. Shimizu, T. Kubo, R. Kishi, H. Takahashi, E. Botek, B. Champagne and M. Nakano, *J. Phys. Chem. Lett.*, 2010, **1**, 937.

29 H. Fallah-Bagher-Shaidaei, S. S. Wannere, C. Corminboeuf, R. Puchta and P. V. R. Schleyer, *Org. Lett.*, 2006, **8**, 863.

30 (*a*) C. Gonzalez and H. B. Schlegel, *J. Chem. Phys.*, 1989, **90**, 2154; (*b*) C. Gonzalez and H. B. Schlegel, *J. Phys. Chem.*, 1990, **94**, 5523.